PAPER

Check for updates

A comparative study of Cu-anchored 0D and 1D ZnO nanostructures for the reduction of organic pollutants in water

Hazim M. Ali,[a] Samia M. Ibrahim,[b] Essam F. Abo Zeid,[c] Ahmed F. Al-Hossainy [b]
and Mohamed Abd El-Aal [*d]

In this work, Cu NPs were loaded at a fixed percentage (5 wt%) on 1D, (1D + 0D) and 0D ZnO nanostructures to investigate the effect of the support morphology on the reduction of organic pollutants in water. The synthesized materials were characterized by high-resolution transmission electron microscopy (HR-TEM), ultraviolet-visible spectroscopy (UV-Vis), Fourier transform infrared spectroscopy (FTIR), X-ray diffraction (XRD), N_2 adsorption–desorption and X-ray photoelectron spectroscopy (XPS). The results reveal that the loading of Cu NPs decreases the optical band gap, and a slight change in the crystallite sizes increases the specific surface area value of the nanocomposites. The TEM images reveal that 1D ZnO has an average width of 44.7 nm and an average length of 211 nm, while 0D ZnO has an average diameter of 54.5 nm. The HR-TEM and XPS data confirm the loading of metallic Cu NPs on the surface of the ZnO nanostructures. The pure ZnO and nanocomposites were tested for 4-nitrophenol (4-NP) reduction in the presence of $NaBH_4$ at room temperature. The obtained results show that pure ZnO nanostructures have no catalytic performance, while the nanocomposites showed good catalytic activities. The catalytic reduction efficiency of 4-NP was found to follow the order of Cu/0DZnO > Cu/(1D + 0D)ZnO > Cu/1DZnO. The complete reduction of 4-NP has been observed to be achievable within 60 s using the Cu/0DZnO nanocomposite, with a k_{app} value of 8.42 min^{-1} and good recyclability of up to five cycles. This nanocomposite was then applied in the reduction of organic dyes in water; it was found that the reduction rate constants for the methylene blue, Congo red, and acriflavine hydrochloride dyes were 1.4 min^{-1}, 1.2 min^{-1}, and 3.81 min^{-1}, respectively. The high catalytic performance of this nanocomposite may be due to the small particle size, high specific surface area, and the high dispersion of Cu NPs on the surface of ZnO.

1 Introduction

Water pollution is mainly caused by the discharge of industrial effluents, which contain substantial amounts of heavy metal ions,[1] nitro aromatic compounds, azo dyes, and hydrolysis products of pesticides and herbicides. Therefore, the elimination of toxic dyes and nitro aromatic compounds should get more attention. The removal of such materials from wastewater is very difficult due to their chemical and biological stability.[2] Moreover, forgoing the utilization of these hazardous materials in human life is difficult because of their use in many important

fields such as pharmaceuticals, textile dyes, paints, plastics, fungicidal agents, and industrial solvents. 4-Nitrophenol (4-NP) and organic dyes in industrial and agricultural wastewater are common organic contaminants, which are very toxic, carcinogenic, and mutagenic to human beings and aquatic organisms. The removal of organic pollutants from water is essential to protect aquatic ecosystems, protect the health of human beings, and solve the problem of water shortage. Thus, it is crucial to develop advanced technologies for the removal of these toxic materials from wastewater.

Different approaches such as electrocatalytic reduction,[3] membrane separation,[4] photocatalytic degradation,[5] ozone oxidation,[6] adsorption[7] and biological treatment[8] have been successfully established for the effective removal of these hazardous compounds or converting them to less toxic species. However, some of these techniques have the following disadvantages: (1) some cannot destroy the pollutants but transfer them from one phase to another, (2) some can degrade the pollutants but they require expensive apparatus, and (3) some methods can also effectively decompose the pollutants;

[a]*Department of Chemistry, College of Science, Jouf University, P.O. Box 2014, Sakaka, Aljouf, Saudi Arabia*

[b]*Chemistry Department, Faculty of Science, New Valley University, El-Kharga, 72511, New Valley, Egypt*

[c]*Physics Department, Faculty of Science, Assiut University, Assiut 71516, Egypt*

[d]*Catalysis and Surface Chemistry Lab, Chemistry Department, Faculty of Science, Assiut University, Assiut, 71516, Egypt. E-mail: dmdsa13@gmail.com; mohamedabdelaal@aun.edu.eg*

however, they use algae, fungi, bacteria, and yeasts, and these are toxic and carcinogenic to microorganisms. The catalytic reduction of these pollutants has been reported as an effective approach for wastewater treatment technology.[9,10] It can effectively degrade pollutants with good stability and recyclability. However, a highly active catalyst is required for effective pollution reduction in the environment.

The use of noble and transition metal nanoparticles-based catalysts as a heterogeneous catalyst for the reductive degradation of organic contaminants is very promising.[11–13] These catalysts have a high density of active catalytic sites due to their recyclability, chemical and physical toughness, and a large surface area. Copper nanoparticles (Cu NPs) exhibit high potential in the field of nanoscience and nanotechnology due to their inexpensive cost and novel physiochemical characteristics; thus, they are being used to replace noble metal NPs. Recently, Cu NPs have been considered as promising catalysts for the oxidation of alcohols,[14] oxidation of CO,[15] C–C bond formation reactions,[16] C–heteroatom bond formation,[17] and various coupling reactions.[18,19] Unfortunately, thermodynamically unstable Cu NPs are prone to coalescence and agglomeration, resulting in a significant reduction in their catalytic activity. Immobilizing Cu NPs on specific supporting substrates, such as carbon materials,[20] porous silica,[21] polymers,[22] metal oxides,[23] and metal–organic frameworks,[24] are the most effective approaches for overcoming this drawback. Catalyst supports serve a critical function in preventing nanoparticle agglomeration and offer a high surface area, which makes it easier to be recovered and reused.[25] Consequently, this prevents the leaching of nanoparticles in the environment and minimizes the cost at the same time. Benefiting from the good loading capacity, geological abundance, ecofriendliness, easy synthesis, and remarkable structural stability, ZnO was widely utilized as a promising catalyst support. In this issue, Rasaki et al.[26] synthesized Ag/ZnO nanorods catalyst, which showed the high catalytic reduction of 4-NP. A Ag/ZnO nanohybrid material was prepared by Oualid et al.[27] using the sodium alginate method for the sonocatalytic reduction of 4-NP and antibacterial activity. The Ag@ZnO/MWCNT nanocomposite was investigated by García-Valdivieso et al.[28] for 4-NP reduction. Behera et al.[29] synthesized maghemite/ZnO nanocomposites for 4-NP reduction. The CuO/ZnO nanocomposite was synthesized in a green manner by the assistance of Melissa officinalis L. leaf extract and investigated for the reduction of 4-NP and Rhodamine B by Bordbar et al.[30] Alamro et al.[31] synthesized ZnO supported on carbon nanotubes for 4-NP reduction via the laser assistance method. The ZnO/CdO thin film for 4-NP catalytic degradation was investigated by Mostafa et al.[32] Alula et al.[33] prepared silver-coated ZnO/Fe$_3$O$_4$ composites for the reduction of 4-NP.

The physicochemical properties of ZnO supports such as effective charge separation, photovoltaic, electron trapping, photoluminescence, Lewis acid/base properties, defect formation, and strong metal–ZnO interactions have been reported to play important roles in catalytic reactions.[34] Their morphologies and nanostructures have a great impact on these properties. The Cu–ZnO interactions influence the interface structure and stability, which contributes significantly to improve its catalytic

properties, such as increasing the available active sites.[35] As a result, studying the effect of the ZnO support shape and its role in the catalytic reduction reaction is of significant interest. However, the influence of the support morphology on the catalytic reduction of 4-NP and organic dyes over Cu NPs/ZnO has not been documented to our knowledge.

In this paper, the effect of the support morphology on the catalytic activity of Cu/ZnO nanocomposites for the reduction of 4-NP was studied. The pure ZnO and Cu/ZnO nanocomposites were characterized via transmission electron microscopy (TEM), UV-Vis spectroscopy, Fourier transform infrared (FTIR) spectroscopy, X-ray diffraction (XRD), surface area, and X-ray photoelectron spectroscopy (XPS). The relationships between the catalytic performance of the nanocomposites with their surface area and their physicochemical properties were determined. The results revealed that the nanocomposite that contains 0D ZnO support showed the highest catalytic performance for the reduction of 4-NP. Moreover, this nanocomposite was applied for the reduction of organic dyes such as methylene blue, Congo red, and acriflavine hydrochloride.

2 Materials and methods

2.1. Chemicals

All materials were of analytical grade and used without any further purification. All solutions were prepared using double-distilled water. Zinc acetate dihydrate (Zn (CH$_3$COO)$_2$·2H$_2$O, assay: 99.5%), sodium hydroxide (NaOH, assay: 99%), potassium hydroxide (KOH, assay: 99%), and L-ascorbic acid (assay: 98%) were purchased from Alpha Chemika. Copper nitrate Cu (NO$_3$)$_2$·3H$_2$O (assay: 98%, Laboratory Chemicals) and 4-nitrophenol (assay: 98%) was supplied by Research-Lab Fine Chem Industries (India), sodium borohydride NaBH$_4$ (assay: 98%) was purchased from SDFCL, while absolute ethanol (ADWIC), methylene blue (MB), Congo red (CR), and acriflavine hydrochloride (ACF) dyes were bought from Sigma-Aldrich (Germany). The chemical structures of 4-NP, MB, CR, and ACF are depicted in Fig. 1.

2.2. Synthesis of ZnO nanoparticles (NPs)

2.2.1. Synthesis of 1D ZnO NPs. 1D ZnO NPs were synthesized by the thermal decomposition method following the method reported by Singh et al.[36] In this method, about 13.50 g Zn(CH$_3$COO)$_2$·2H$_2$O was grounded in an agate mortar and pestle for one hour. The powder was then annealed in a muffle furnace at 500 °C for 3 h with a ramping rate of the furnace of 3 °C per minute.

2.2.2. Synthesis of (1D + 0D) ZnO NPs. (1D + 0D) ZnO NPs were synthesized via the microwave-assisted method following the method reported by Nikhil et al.[37] In a typical synthesis, about 13.50 g Zn(CH$_3$COO)$_2$·2H$_2$O and 51.75 g KOH were dissolved in 100 mL double-distilled water and stirred at room temperature for 20 min. The mixture was then transferred to a scientific microwave oven (Start Synth) flask and irradiated for 20 min at 360 W power and 180 °C reaction temperature. The obtained precipitate was filtered off and rinsed twice using double-
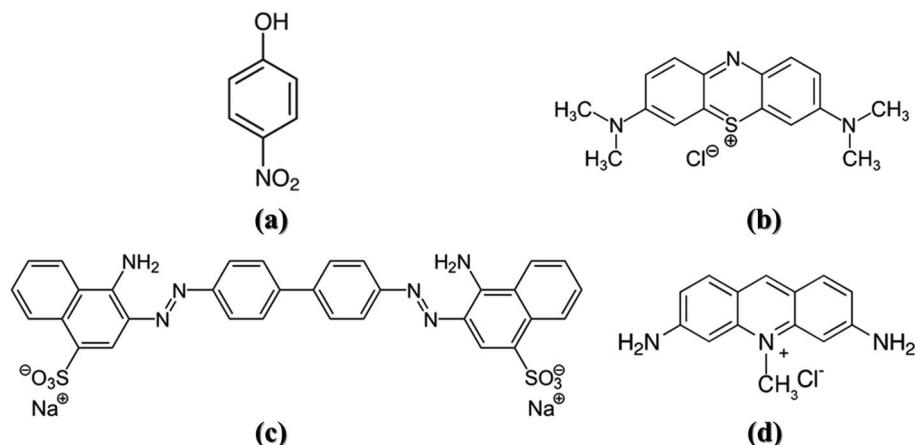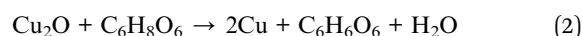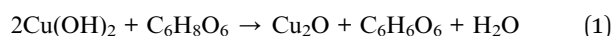
Fig. 1 The chemical structures of (a) 4-nitrophenol, (b) methylene blue, (c), Congo red, and (d) acriflavine hydrochloride.

distilled water and ethanol to remove any impurities. Then, the collected precipitate was dried overnight at 80 °C and subjected to calcination at 500 °C for 1 h in a static air atmosphere.

2.2.3. Synthesis of 0D ZnO NPs. ZnO NSs were synthesized by the chemical precipitation method following the conditions reported by Cao *et al.*[38] In the preparation method, about 13.50 g $Zn(CH_3COO)_2 \cdot 2H_2O$ was dissolved in about 500 mL ethanol and named as solution (A). Solution (B) was prepared by dissolving about 14.76 g of NaOH in a mixture of ethanol and water (78 : 1 *V/V*). Solution (B) was added dropwise to solution (A) with vigorous stirring for 2.25 h at 60 °C. The resulting precipitate was filtered off and thoroughly washed with double-distilled water and ethanol once the solution had cooled to room temperature. The precipitate was then dried overnight at 80 °C and calcined for 1 h in a static air atmosphere at 500 °C.

2.3. Synthesis of the Cu/ZnO nanocomposite

A calculated amount of $Cu(NO_3)_2 \cdot 3H_2O$ corresponding to the theoretical yield of ZnO NPs, 5% (*w/w*), was respectively dissolved in 100 mL double-distilled water with stirring at room temperature. An amount of ZnO NPs powder was dispersed in copper nitrate solution (pH = 3.3) with sonication for 15 min. The solution pH was changed to 8.52 after the complete dispersion of ZnO NPs, which indicates the formation of $Cu(OH)_2$.[39] After that, about 50 mL L-ascorbic acid solution ([L-ascorbic acid] = 5[$Cu(NO_3)_2 \cdot 3H_2O$]) was added dropwise into the above mixture with continuous stirring at 90 °C for 2.5 h. The pH of the mixture was changed to 5.54 after the complete addition of the L-ascorbic acid solution, which confirmed the transformation of $Cu(OH)_2$ to Cu NPs through the formation of Cu_2O as an intermediate.[39] The precipitate was filtered out and rinsed with ethanol and double-distilled water multiple times when the solution cooled to room temperature. Finally, the precipitate was dried for 5 h at 80 °C. The formation of Cu NPs on the surface of ZnO support is expected to follow these steps. Cu^{2+} ions were first converted to $Cu(OH)_2$, which was subsequently reduced to Cu_2O by L-ascorbic acid. Finally, Cu_2O was converted to Cu particles. The reduction process can be represented as follows:[39]

$$2Cu(OH)_2 + C_6H_8O_6 \rightarrow Cu_2O + C_6H_6O_6 + H_2O \qquad (1)$$

$$Cu_2O + C_6H_8O_6 \rightarrow 2Cu + C_6H_6O_6 + H_2O \qquad (2)$$

2.4. Characterization techniques

The morphologies of the pure ZnO nanostructures and the Cu/ZnO nanocomposites were determined by transmission electron microscopy (TEM, JSM-2100 JEOL, Japan) operated at an acceleration voltage of 200 kV.

The optical properties of the Cu/ZnO nanocomposites were checked by recording the UV-Vis spectra of the aqueous suspension of each sample using a SHIMADZU UV-3101 UV-Vis-NIR spectrometer at room temperature.

The surface functionality and presence of organic impurities was estimated *via* FTIR spectroscopy (Nicolet spectrophotometer, model 6700) using the KBr pellet technique in the 400–4000 cm^{-1} range.

The phase and crystal structure of Cu/ZnO nanocomposite were investigated using X-ray diffraction technique (XRD, Philips diffractometer, model PW 2103/00) equipped with a Ni-filtered Cu Kα radiation (λ = 1.5408 Å). The samples were scanned over 4–80° of the 2θ range at a scan rate of 3° min^{-1}.

The surface area and texture of the catalysts were determined *via* N$_2$ adsorption at −196 °C using a Nova 3200 gas adsorption apparatus (Quantachrom Instrument Corporation, USA). The Brunauer–Emmett–Teller (BET) theory was used to calculate the surface area.

X-ray photoelectron spectroscopy (XPS) measurements were obtained on a K-ALPHA instrument (Thermo Fisher Scientific, USA) with monochromatic X-ray Al K-alpha radiation in the range from −10 to 1350 eV with a spot size of 400 μm at a pressure of 10^{-9} mbar with a full spectrum pass energy of 200 eV and at narrow spectrum of 50 eV.

2.5. Catalytic reduction of 4-NP

The reduction of 4-NP to 4-aminophenol (4-AP) as a model reaction in the presence of excess NaBH$_4$ was used to investigate

the catalytic characteristics of the Cu/ZnO nanocomposites. Briefly, about 0.3783 g $NaBH_4$ was dissolved in 100 mL double-distilled water in 250 mL beaker; then 1 mL 4-NP (1×10^{-2} M) solution was added, and then the solution mixture changed from colorless to intense yellow.[40] UV-Vis spectroscopy in the wavelength range of 200–600 nm was used to monitor the reaction progress using a small amount of the reaction mixture after a certain time interval. In the reaction process, the catalytic conversion efficiency of 4-NP to 4-AP could be calculated using the formula.

$$\text{Conversion efficiency of 4 -NP}(\%) = \frac{A_0 - A_t}{A_0} \times 100 \quad (3)$$

where A_0 is the 4-nitrophenolate anions' initial absorbance at $\lambda_{max} = 400$ nm, while A_t is the absorbance at different time (t) intervals.

3   Results and discussion

3.1.   Characterization of Cu/ZnO nanocomposites

The morphologies of pure ZnO nanostructures and Cu/ZnO nanocomposites were observed by TEM. As shown in Fig. 2a of 1D ZnO, the sample has rod-like particles with an average width of 44.7 nm and an average length of 211 nm. Fig. 2b shows the micrograph of (1D + 0D) ZnO; the polydispersed nanostructure contains rod particles with an average width and length of 38.1 nm and 149.5 nm, respectively. Semi-spherical particle with an average diameter of 54.5 nm were observed from Fig. 2c of 0D ZnO. Also, the same morphology of semi-spherical particles of the Cu/0DZnO nanocomposite was obtained (Fig. 2d). The HR-TEM image of the Cu/0DZnO nanocomposite (Fig. 2e) showed a lattice spacing of 0.26 nm and 0.21 nm corresponding to the d-spacing of ZnO (002)[41] and Cu
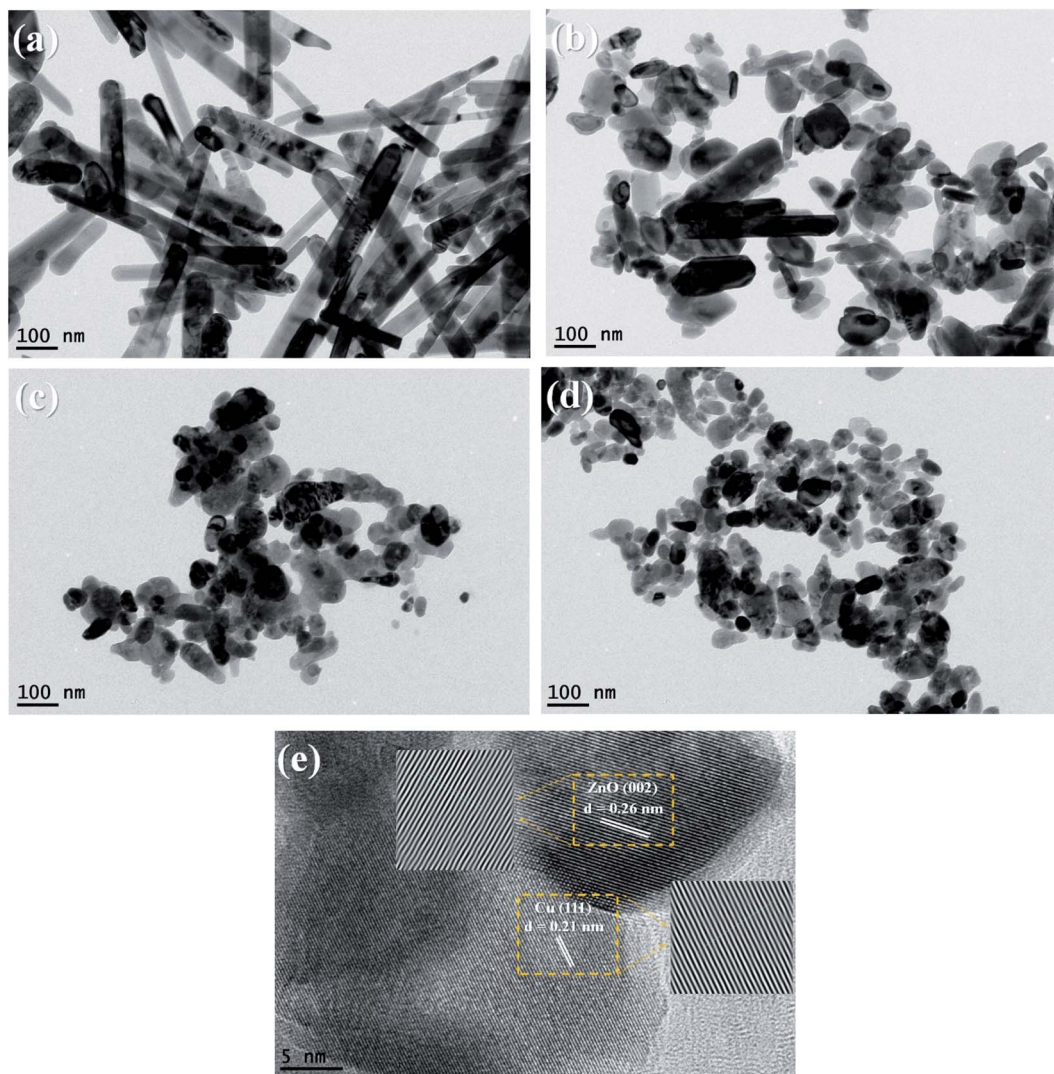

Fig. 2   TEM images of (a) 1D ZnO, (b) (1D + 0D) ZnO, (c) 0D ZnO, (d) the Cu/0DZnO nanocomposite, and (e) the HR-TEM image of the Cu/0D ZnO nanocomposite.

(111),[42] respectively. EDX mapping analysis was used to study the elemental distribution of Cu, Zn, and O in the Cu/0D nanocomposite (Fig. 3a–e). It can be observed that the Cu NPs was successfully loaded and uniformly distributed on the surface of the ZnO support.

As shown in Fig. 4, as a nondestructive tool, diffused reflectance spectroscopy (DRS) was utilized to characterize the optical parameters of ZnO nanostructures and Cu/ZnO nanocomposites with infinite thickness. By utilizing the Kubelka–Munk model, the prepared nanocomposites' photocatalyst band gap was evaluated from the DRS data. From the curve between $(F(R)E)^2$ and E, the optical band gap is estimated according to Kubelka–Munk and Tauc's equations.[43,44] The optical band gap was estimated from the x-axis at the intercept
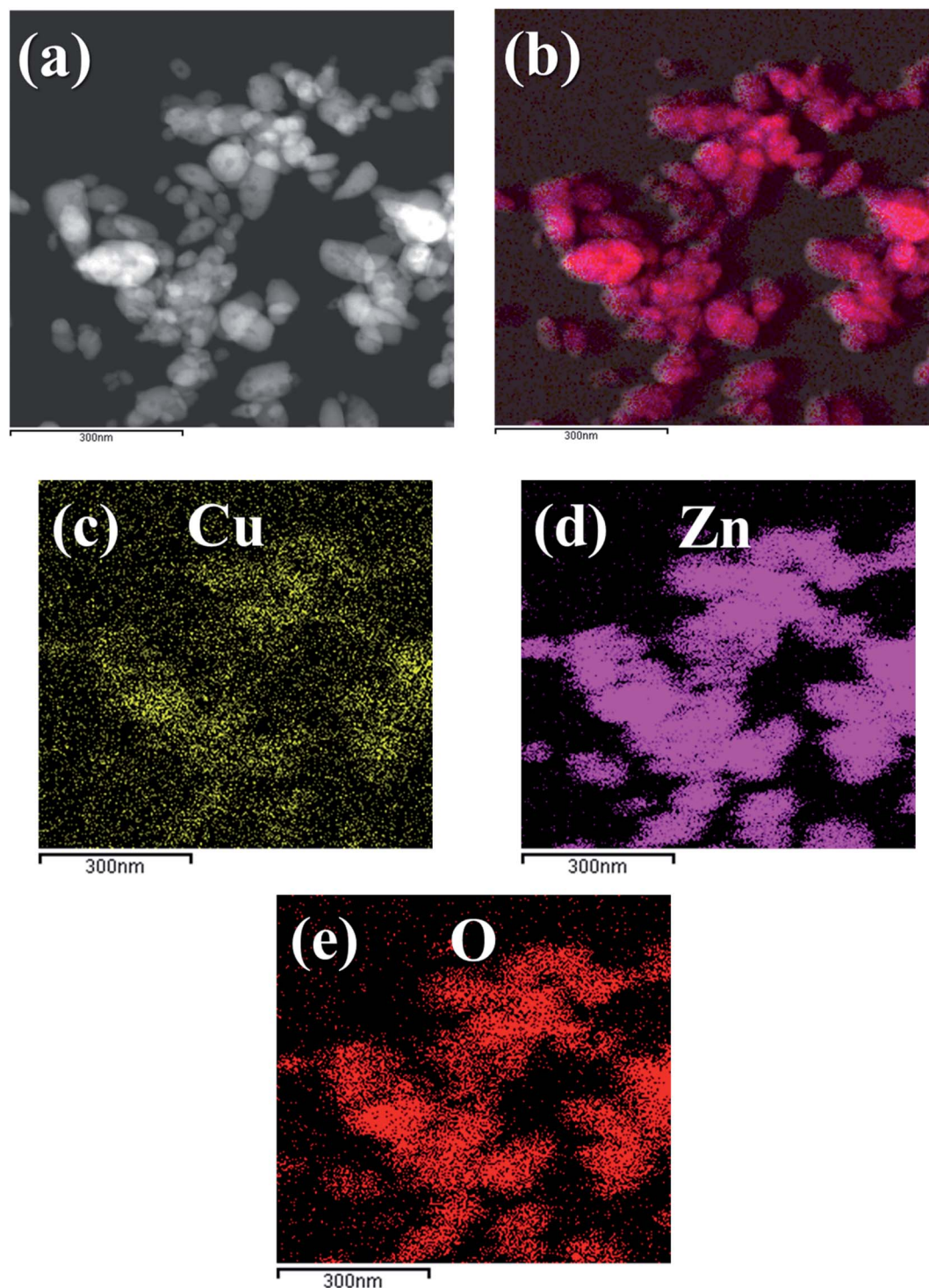

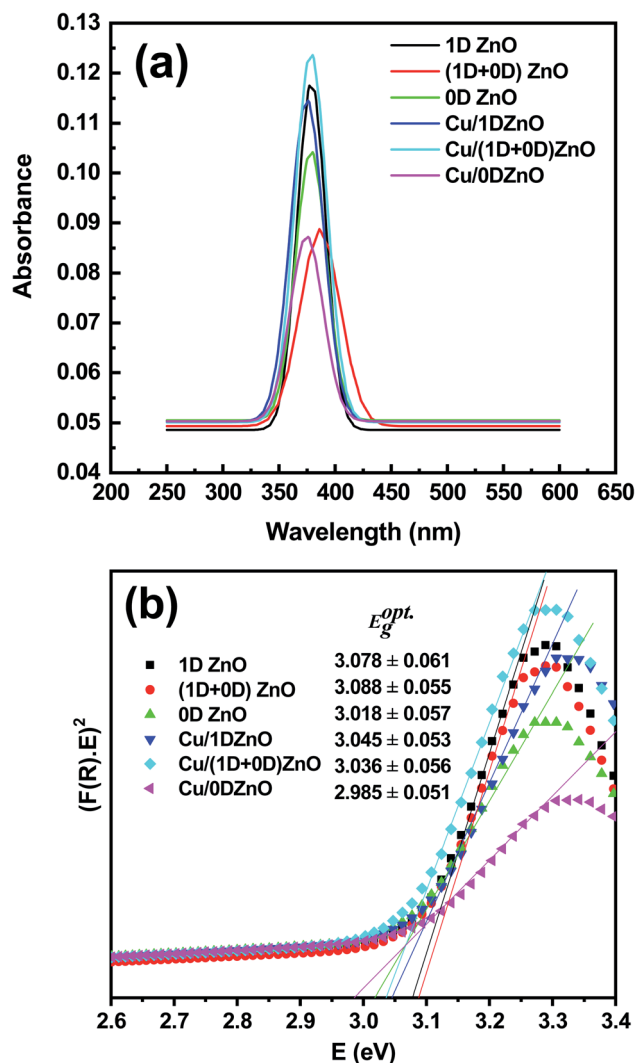**Fig. 3** EDX mapping images of the Cu/0DZnO nanocomposite.

Paper

Fig. 4 (a) UV-vis diffuse reflectance spectra of the ZnO nano-structures and Cu/ZnO nanocomposites, and (b) the determination of their band gap.

3.21 eV (ZnO) to 3.07 eV ($Zn_{0.9}Cu_{0.1}O$); these values are similar to our results. In addition, these impurities created a special imperfection, which seems to raise the Fermi level toward the conduction band.[47,48] The light absorption in the semi-conductor nanocomposites results in the transportation of the valence band electrons to a particular state through the conduction band to provide electron in the conduction band and hole in the valence band. If the size of the nanoparticle is equal to the de Broglie wavelength, then the conduction band is regarded as a quantum cavity of the electrons. According to the obtained results, we can conclude that the optical band gap of the prepared semiconductor nanocomposites could be affected by its morphological changes, and demonstrated a prospective agent for photovoltaics and other optical applications.

FTIR studies were performed to ascertain the purity and nature of the functional groups available on the Cu/ZnO nanocomposites. The FTIR spectra of the ZnO nanostructures and Cu/ZnO nanocomposites are depicted in Fig. 5. The pristine 1D and (1D + 0D) ZnO nanostructures exhibited almost the same bands. They showed bands for functional groups located at 3412 cm^{-1}, 2922 cm^{-1}, 2852 cm^{-1}, 2359 cm^{-1}, 2341 cm^{-1}, 1561 cm^{-1}, 1383 cm^{-1}, 871 cm^{-1}, and 421 cm^{-1}. The band located at 3412 cm^{-1} is assigned to the stretching vibration of the OH groups, which resulted from water molecules adsorbing on the ZnO surface. The asymmetric and symmetric (C–H) vibration modes of acetate CH_2 groups were detected at 2922 cm^{-1} and 2852 cm^{-1}.[49] The vibration bands at 2359 cm^{-1} and 2341 cm^{-1} are assigned to atmospheric CO_2.[50] The bands ranging from 1561 cm^{-1} to 1383 cm^{-1} are attributed to the symmetric and asymmetric stretching vibration of the C=O group,[51] which may be due to zinc acetate used in the reaction. The bands detected at 871 cm^{-1} and 421 cm^{-1} are attributed to the stretching vibrational mode of the metal–oxygen bond (Zn–O).[52] In addition to the bands showed by 1D and (1D + 0D) ZnO, 0D ZnO exhibited three signals at 1775 cm^{-1}, 1436 cm^{-1}, and 880 cm^{-1}, which could be because of the adsorbed carbonate

with an extended straight line. The calculated values of the optical band gaps for 1D, (1D + 0D), 0D ZnO, Cu/1D, (1D + 0D), and 0D ZnO were found to be 3.078 ± 0.061 eV, 3.088 ± 0.055 eV, 3.018 ± 0.057 eV, 3.045 ± 0.053 eV, 3.036 ± 0.056 eV, and 2.985 ± 0.051 eV, respectively. It was noted that the loading of Cu NPs on ZnO nanostructures leads to a decrease in the optical band gap of the nanocomposite, which results in absorption edge redshift. The decrease in the optical band gap energy could be attributed to high density oxygen vacancies and syndromes corresponding to the difference in the ionic radius and electronegativity between the Cu and ZnO ions because of the substitution procedure of Zn^{2+} by Cu^{2+} in the matrix. E. Gurger et al. have evaluated the optical band gap of ZnO to be 3.24 eV and by introducing Ag and Cu impurity atoms in the nanocomposite, the band gap narrowed to 3.18 eV and 3.12 eV for ZnO–Cu and ZnO–Ag, respectively.[45] Chakraborty et al.[46] found that copper doping decreases the electron–hole recombination, and the optical band gap value was reduced from
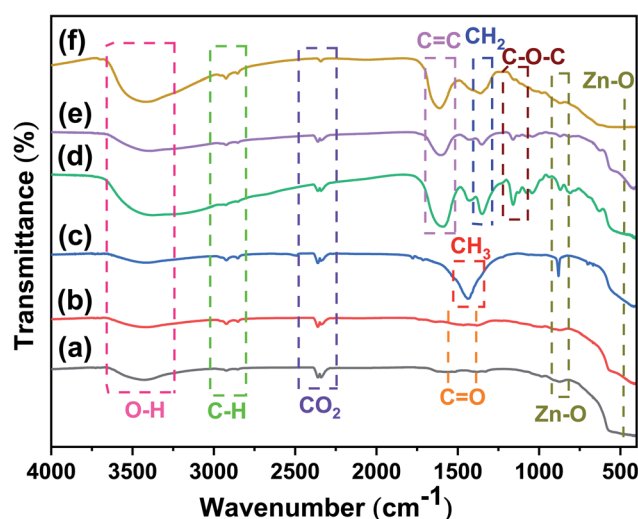

Fig. 5 FTIR spectra of (a) 1D ZnO, (b) (1D + 0D) ZnO, (c) 0D ZnO, (d) Cu/1DZnO, (e) Cu/(1D + 0D)ZnO, and (f) Cu/0DZnO.

moieties,[53] the in-plane bending vibrations of the methyl group (CH_3),[54] and the metal–oxygen bond (Zn–O) stretching vibrational mode,[52] respectively. The differences in the bands positions and intensities for the acetate group may be due to the different amounts of acetate adsorbed on the ZnO surface. The FTIR spectra of Cu/ZnO nanocomposites showed that some bands are similar to pristine ZnO, while some new bands emerged. These new bands were detected at 1605 cm^{-1}, 1427 cm^{-1}, 1350 cm^{-1}, 1160 cm^{-1}, 1076 cm^{-1}, and 1043 cm^{-1}, which might be attributed to the presence of L-ascorbic acid[55] since the reaction occurs under an excess of it. It was also noted that the band intensity of the hydroxyl group in the nanocomposite is sharper than that of pure ZnO.

The XRD patterns of the ZnO nanostructures and Cu/ZnO nanocomposites are shown in Fig. 6. The clear, intense diffraction peaks indicate the extremely crystalline quality of the grown nanoparticles. After the analysis of positions and comparative intensities of the diffracted peaks, the occurrence of single-phase hexagonal wurtzite of ZnO with space group $P6_3mc$ was established.[56] The XRD patterns of the ZnO nanostructures were similar, except for the variation in line broadening due to the change in the morphologies. The pristine ZnO

nanostructures exhibit well-defined XRD peaks at $2\theta = 31.8°$, 34.5°, 36.3°, 47.6°, 56.7°, 62.9°, 66.5°, 68°, 69.2°, 72.6°, and 77°, which are corresponding to the (100), (002), (101), (102), (110), (103), (200), (112), (201), (004), and (202) crystal planes, respectively. All the diffraction peak positions and their corresponding crystal planes are described by the standard spectrum (JCPSD card no. 01-089-0511).[57] In addition, no additional reflections can be detected related to the other impurities, indicating the high purity of the produced ZnO. On the other hand, the XRD patterns of Cu/ZnO nanocomposites showed typical reflections of the pristine ZnO nanostructures. Moreover, a new reflection was noticed at $2\theta = 42.7°$ (for Cu/1D and 0D ZnO) and 42.2° (for Cu/(1D + 0D) ZnO), which corresponded to (111), the preferred oriented plane of the FCC structure of Cu NPs, and no obvious reflections arising from possible impurity phases such as CuO and Cu_2O were detected. The Scherrer equation was used to determine the average crystallite size of the ZnO nanostructures.

$$D = \frac{0.94\lambda}{\beta \cos\theta} \quad (4)$$

where D is the particle crystallite size, λ is the diffraction wavelength ($\lambda = 1.5408$ Å), β is the full width at half maximum of the diffraction peak, and θ is the angle of reflection. The average crystallite sizes were calculated to be 21.53 nm, 23.38 nm, and 19.10 nm for 1D, (1D + 0D), and 0D ZnO, respectively.

To establish the level of defects within the matrix crystal, the dislocation density (δ) was estimated from the following equation.

$$\sigma = \frac{1}{D^2} \quad (5)$$

Corresponding to interior lattice straining and Williamson–Hall equations,[30] the micro-diffraction (ε) in the crystal nanostructure and the crystallite size were evaluated from XRD by:

$$\varepsilon = \frac{\beta_{hkl}}{4 \tan\theta} \quad (6)$$

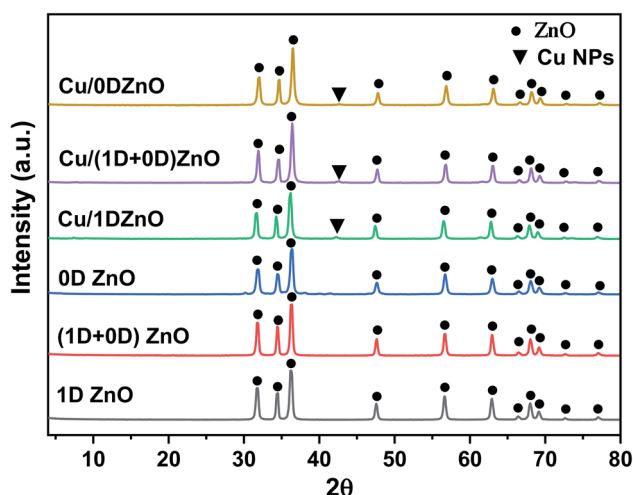$$\beta_{hkl} \cos\theta = 4\varepsilon \sin\theta + \frac{k\lambda}{D} \quad (7)$$

Fig. 6 XRD diffraction patterns of the ZnO nanostructures and Cu/ZnO nanocomposites.

Table 1 Crystal lattice factors and specific surface area values of the ZnO nanostructures and Cu/ZnO nanocomposites

| Samples	Average crystallite size D (nm)				
		Williamson–Hall equation			
	Scherrer's equation (D)	(D)	Microstrain (ε) $\times 10^{-4}$	Dislocation density (δ) $\times 10^{-4}$ (lines nm^{-2})	S_{BET} (m^2 g^{-1})
1D ZnO	22.50	19.60	−5.95789	19.75	10.1
(1D + 0D) ZnO	24.42	22.73	−2.74854	16.77	29.0
0D ZnO	19.95	18.12	−4.65576	25.12	23.9
Cu/1DZnO	22.90	21.52	−2.32384	19.07	17.2
Cu/(1D + 0D)ZnO	22.95	21.87	−7.14024	18.98	35.5
Cu/0DZnO	22.00	22.14	0.534299	20.66	36.1

Table 2 Comparison of the activity of the most active catalyst (Cu/0DZnO nanocomposite) with other Cu catalysts published in the literature

Catalyst	k ($\times 10^{-3}$ s^{-1})	TOF ($\times 10^{-6}$ mmol mg$_{Cu}^{-1}$ s^{-1})	Ref.
Cu NPs	1.59	0.08	64
Cu/polymers	2.10	2.82	65
Hierarchical Cu microspheroids	4.65	0.33	66
Porous Cu microspheres	5.26	9.26	67
Cu nanopolyhedrons	5.70	6.48	68
Hollow porous Cu NPs	9.30	12.8	69
Cu nanoplates	9.50	31.7	70
Cu nanocubes	10.1	11.1	68
Cu NPs-aggregated cages	10.4	34.7	71
Cu/carbon	13.0	3.05	72
Cu/rGO	17.3	104.4	73
Cu/carbon	24.0	3.51	74
Cu/rGO	23.2	298.7	63
Cu/0DZnO	140.4	300	This work

where D and ε were calculated by utilizing the fitting of least square $\beta_{hkl} \cos \theta$ *vs.* $4 \sin \theta$ for estimating the gradient and intercept.

From the results of Table 1, we can note that the average crystallite size of the (1D + 0D) ZnO sample is larger than both that of 1D ZnO and 0D ZnO, respectively, as pure nanostructures. Although the amount of copper added to the zinc

oxide samples of different shapes is a fixed percentage of 5%, we note that the difference in size is not significant, *i.e.*, 22.90 nm, 22.95 nm, and 22.00 nm, respectively. Therefore, the decrease in the crystallite size after adding Cu NPs to zinc oxide is attributed to the difference in the radius between the added copper atom and the host zinc atoms. The incompatibility in the volumes of zinc and copper atoms led to a strain caused by non-uniform
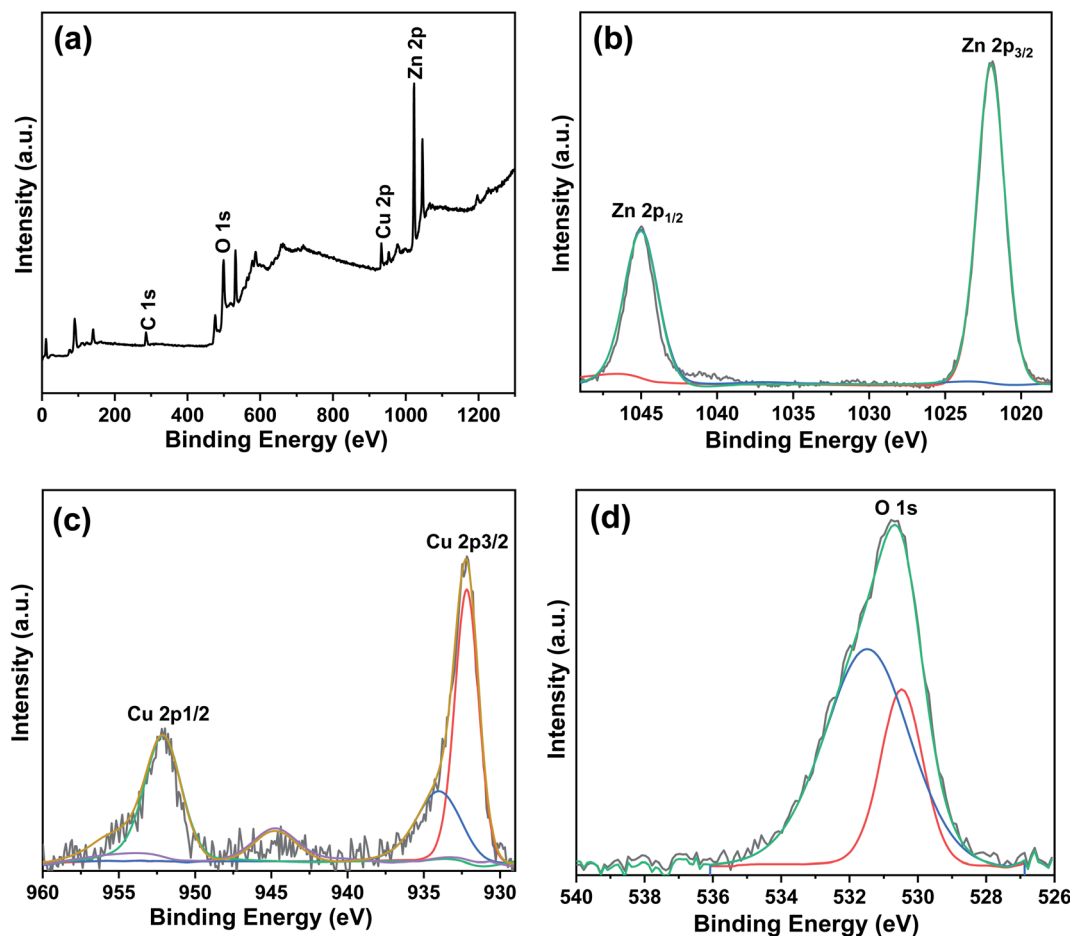
Fig. 7 XPS spectra of the Cu/0DZnO nanocomposite: (a) full survey spectrum, (b) Zn 2p spectrum, (c) Cu 2p spectrum, and (d) O 1s spectrum.

lattice deformation and dislocation in the crystal phase, which appeared in the broadening of the peak in the nanocomposite. In the case of 1D ZnO, adding copper to its crystals increases the micro-strain of the crystal because the nature of stacking the atoms in the form of rods decreases the interatomic distances during the stacking process, which makes the copper atoms substitute in the crystal sparsely. For (1D + 0D) zinc oxide crystals of larger size, adding copper decreases the micro-strain of the lattice crystal, which might be due to the nature of the mixed particles and how the atoms are packed. The increase in the inside crystal lattice strain of zinc oxide's spherical shape might be due to the presence of rather large interspaces within the spherical crystal nanostructure.

The N_2 adsorption–desorption isotherms (not shown) of ZnO nanostructures and Cu/ZnO nanocomposites, as obtained from Brunauer–Emmett–Teller (BET) analysis, are type II, according to the IUPAC classification. The calculated specific areas of all the catalysts are cited in Table 2. The S_{BET} of 1D ZnO, (1D + 0D) ZnO, 0D ZnO, Cu/1DZnO, Cu/(1D + 0D)ZnO, and Cu/0DZnO was about 10.1, 29.0, 23.9, 17.2, 35.5, and 36.1 $m^2\ g^{-1}$, respectively. It is well known that the S_{BET} increases with decreasing particle size and increases if the particles are multi-particle agglomerates or have a rough surface structure.[58] Among the prepared

samples, 1D ZnO has a larger particle size (Fig. 2a) than that of the other samples, and thus, it has the smallest S_{BET} value. Although (1D + 0D) ZnO has a particle size larger than that of 0D ZnO, it has a higher S_{BET} value because it has multi-particle agglomerates (Fig. 2b). It was observed that the addition of Cu NPs to ZnO materials enhances their specific surface area due to the doping effect and the formation of new pores due to effective Cu species diffusion in the ZnO support.[59] The observed increase in the surface area would be helpful for improving the catalytic activity of the nanocomposite catalyst.

The chemical states and surface compositions of the Cu/0DZnO nanocomposite were examined using XPS, and the results are shown in Fig. 7. The full survey spectrum in Fig. 7a indicates the presence of Zn, Cu, O, and C. The high-resolution spectrum for the Zn 2p region (Fig. 7b) shows two peaks at binding energies of 1044.8 eV and 1021.9 eV assigned to Zn $2p_{1/2}$ and Zn $2p_{3/2}$, respectively. The two peaks are separated by a spin-energy of 23 eV, indicating the existence of Zn in the +2 oxidation state.[60] The narrow spectrum of Cu 2p reveals two main binding energy peaks at 952.1 eV and 932.2 eV, which correspond to the $2p_{1/2}$ and $2p_{3/2}$ spin system of zerovalent Cu, respectively.[42] Moreover, two peaks at binding energies of 944.7 eV and 934 eV as characteristics of Cu^{2+} were also
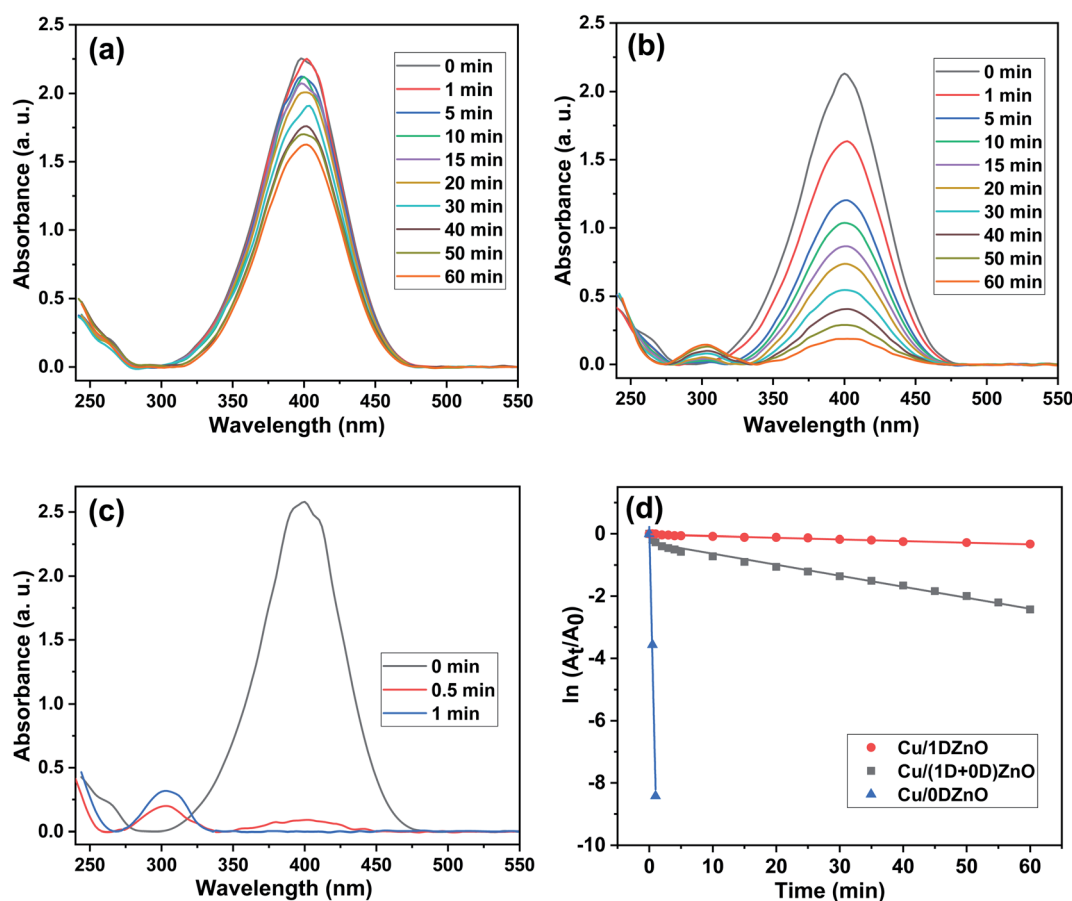

Fig. 8 UV-Vis spectra of the reduction of 4-NP using (a) the Cu NPs/1DZnO nanocomposite as a catalyst, (b) Cu NPs/(1D + 0D)ZnO nanocomposite as a catalyst and (c) Cu NPs/0DZnO nanocomposite as a catalyst, and (d) plots of ln(A_t/A_0) *versus* reaction time in the presence of the Cu/ZnO nanocomposites as catalysts.

detected, which indicates the formation of CuO during the synthesis of Cu NPs.[61] Fig. 7d displays the O 1s spectrum, which was divided into two peaks with binding energies of 531.5 eV and 530.5 eV indexed to chemisorbed oxygen species and lattice oxygen in ZnO, respectively.[62]

3.2. Catalytic performance of Cu NPs/ZnO nanocomposites

3.2.1. Catalytic reduction of 4-NP to 4-AP.
In the presence of excess NaBH$_4$, the catalytic performance of Cu/ZnO nanocomposites was examined for the liquid phase reduction of 4-NP to 4-AP as a model reaction. The aqueous phase solution of 4-NP shows a noticeable absorption peak at $\lambda_{max} = 317$ nm in the UV-Vis spectrum. After the injection of excess NaBH$_4$, this absorption peak was redshifted to 400 nm due to the formation of 4-nitrophenolate ions with a dark yellow color. The position and intensity of the peak at 400 nm remain unchanged without the catalyst. The decrease in the 4-nitrophenolate ion absorption peak ($\lambda_{max} = 400$ nm) and the simultaneous appearance of a new peak of 4-AP at $\lambda_{max} = 300$ nm indicated that the reduction reaction had proceeded. Using a UV-Vis spectrophotometer, the decline in the absorption peak at 400 nm was measured at regular intervals. The UV-Vis spectra during the reduction of 4-NP over Cu/ZnO nanocomposites are presented in Fig. 8. In the presence of pristine ZnO nanostructures, there was no discernible change in the absorption peak at $\lambda_{max} = 400$ nm after 1 h, which indicated that they have no catalytic activity for 4-NP reduction. These results are in agreement with those obtained by Bordbar *et al.*[30] However, the decline in the absorption peak at 400 nm and the yellow color of the mixture started to disappear after the addition of Cu NPs/ZnO nanocomposites in the reaction mixture. The Cu/0DZnO nanocomposite showed outstanding catalytic performance with 4-NP reduction efficiency of about 100% in 1 min, while the Cu/(1D + 0D)ZnO nanocomposite exhibited a reduction efficiency of 91% in 1 h. On the other hand, the Cu/1DZnO nanocomposites demonstrated a poor catalytic efficiency of 28% in 1 h. The Cu/0DZnO nanocomposites have a high catalytic performance due to their high specific surface area, small particle size, and excellent dispersion of Cu NPs on the ZnO surface, which provide more active sites for the reduction reaction.

Because the concentration of NaBH$_4$ is substantially higher than that of 4-NP, the reaction is thought to follow pseudo first order kinetics, as shown by the equation

$$\ln \frac{A_t}{A_0} = -k_{app}t \tag{8}$$

where A_0 is the absorbance of 4-nitrophenolate ion ($\lambda_{max} = 400$ nm) at zero time, A_t is the absorbance at different time intervals, k_{app} is the apparent reaction rate constant, and t is the reaction time. Fig. 8 shows the plot of $\ln(A_t/A_0)$ *versus* time (t) and the kinetic data of 4-NP reduction catalyzed by Cu/1D, (1D + 0D), and 0D ZnO nanocomposites. The calculated rate constants were 0.00523, 0.03546, and 8.42 min^{-1} for Cu/1D, (1D + 0D), and 0D ZnO nanocomposites, respectively. Furthermore, the value of turnover frequency (TOF, mmol mg$_{Cu}^{-1}$ s^{-1}) was estimated by the following equation.[63]

$$\mathrm{TOF} = \frac{N_{4\text{-NP}}}{M_{Cu}t} \tag{9}$$

where N (mmol) is the concentration of 4-NP, M (mg) represents the amount of Cu NPs, and t (s) is the reaction time. The comparison of the catalytic activity of the most active catalyst (Cu/0DZnO) with other Cu catalysts found in the literature is given in Table 2. The comparison indicates that the Cu/0DZnO nanocomposite has higher k and TOF values (300×10^{-6}) than those of the other catalysts. The high catalytic activity of this catalyst may be due to the high specific surface area, ultrafine size, and good dispersion of Cu NPs.

Based on the previous investigations,[75,76] the catalytic reduction of 4-NP over Cu/0DZnO nanocomposite is an electron transfer process and proceeded *via* two steps. The BH$_4^-$ ions were first diffused from the solution to the surface of the Cu NPs, forming a Cu-hydride complex *via* π–π stacking interactions. Meanwhile, 4-NP was reversibly adsorbed on the surface of Cu NPs. Then, electron transfer occurred from BH$_4^-$ and 4-
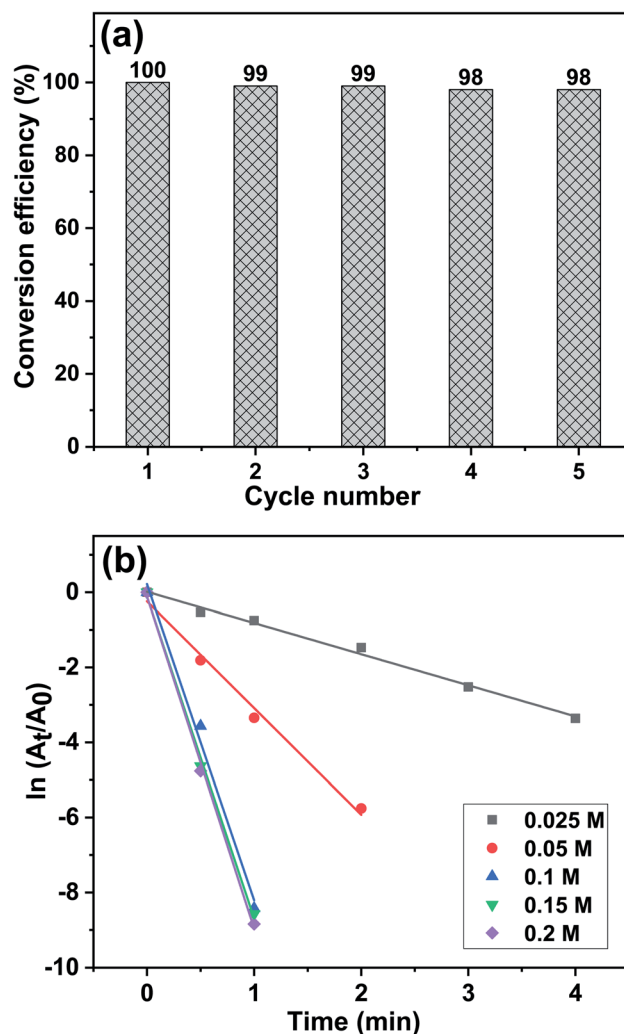

Fig. 9 (a) Recyclability of the Cu/0DZnO nanocomposite towards catalytic 4-NP reduction, and the (b) relationship between $\ln(A_t/A_0)$ and reaction time and under various NaBH$_4$ concentrations in the presence of the Cu/0DZnO nanocomposite as a catalyst.

NP near the surface of the Cu NPs supported on ZnO as the electron mediator. The hydrogen was transferred from the Cu hydride complex to the nitro group, which was then reduced. The final product (4-AP) was desorbed from the surface of the nanocomposite. We may deduce from the previous explanation that the ZnO support can stabilize Cu NPs against aggregation and boost the reduction activity *via* a synergistic action.

Stability and reusability are important factors for a catalyst's practical application. To investigate if the Cu/0DZnO nanocomposite could be reused, five successive cycles were carried out using 0.01 g of the catalyst; the results are shown in Fig. 9a. After each cycle, the catalyst was filtered out of the reaction mixture, washed several times with double-distilled water and ethanol, and dried at 60 °C in an oven. Only a slight decrease in the catalytic activity of the nanocomposite was observed after five cycles. The primary cause of the decline in the catalytic activity is the loss of small portions of the catalyst during the separation process.

The effect of NaBH$_4$ concentration variation (0.05 M to 0.2 M) on the catalytic performance of the Cu/0DZnO nanocomposite for the reduction of 4-NP was investigated while keeping the 4-NP concentration constant (0.1 mM). The plot of $\ln(A_t/A_0)$ against time for every concentration of NaBH$_4$ tested is displayed in Fig. 9b. It was found that when NaBH$_4$ concentration shifts from 0.05 M to 0.2 M, the k_{app} increases from 0.38 min^{-1}

to 8.84 min^{-1}. With increasing concentration of NaBH$_4$, the produced BH$_4^-$ is increased, and more electrons are delivered to the 4-NP; thus, the reduction occurs rapidly with a higher k_{app} value and *vice versa*.[77]

3.2.2. Catalytic reduction of methylene blue (MB). MB is a cationic dye that is utilized in the textile, paper, rubber, and plastic sectors and causes substantial environmental damage.[78] The absorption peaks of MB in aqueous solution are 664 nm and 614 nm. In a typical catalytic reaction procedure, 0.3783 g NaBH$_4$ was dissolved in 100 ml double-distilled water in a 250 mL beaker, then 100 μL of MB (1×10^{-2} M) solution was added. Fig. 10a shows the UV-Vis spectrum of MB reduction by NaBH$_4$ in the presence of 0.01 g Cu/0DZnO nanocomposite. It has been noted that the intensities of the peaks for MB gradually decrease with time and fully disappear after 2 min. The presence of Cu/0DZnO nanocomposite as the catalyst helps in the electron transfer from BH$_4^-$ (donor) to MB (acceptor). The reaction follows pseudo first order kinetics because the concentration of NaBH$_4$ is substantially higher than that of MB, and the linear relationship between $\ln(A_t/A_0)$ and time (t) is depicted in Fig. 10d. The reaction's rate constant was estimated from the straight line's slope and was found to be 1.4 min^{-1}.

3.2.3. Catalytic reduction of Congo red (CR). CR is a very poisonous and carcinogenic anionic dye that is widely employed in a variety of industries, including textiles, printing,
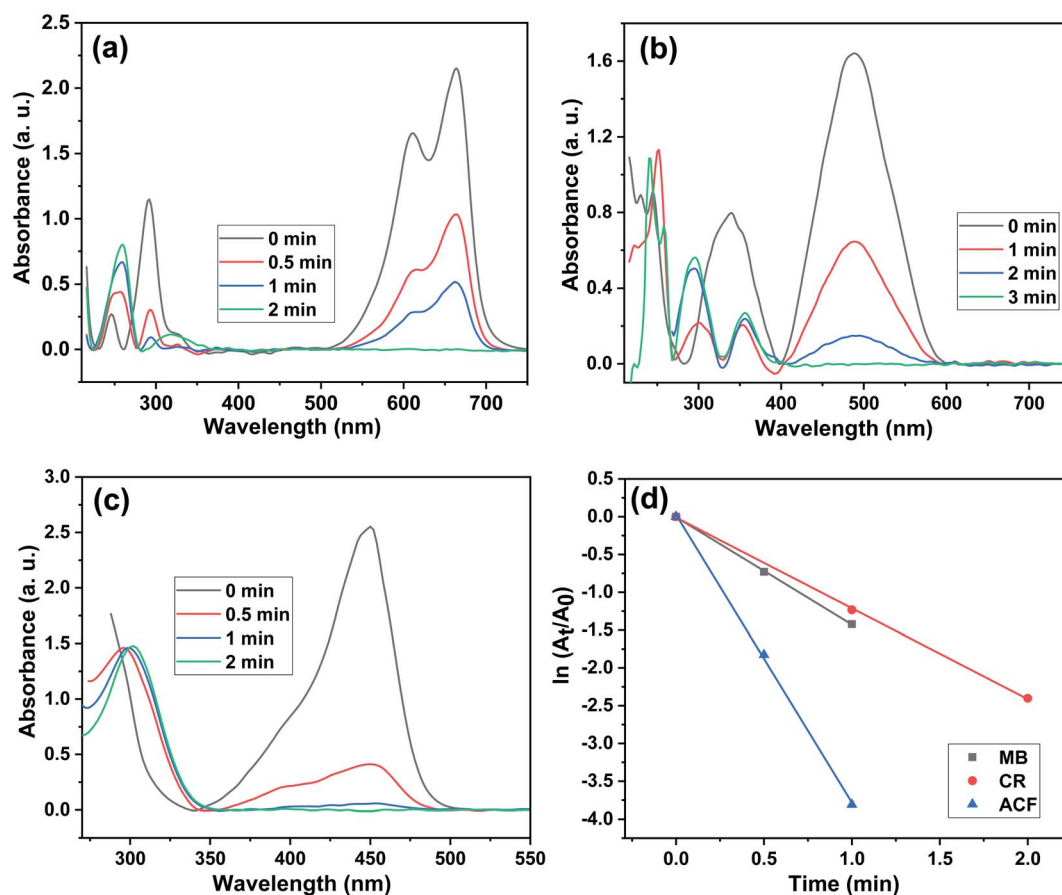

Fig. 10   UV-Vis spectra of the reduction of (a) MB, (b) CR, and (c) ACF using the Cu/0DZnO nanocomposite as a catalyst, and (d) plots of $\ln(A_t/A_0)$ *versus* reaction time in the presence of the Cu/0DZnO nanocomposite as a catalyst.

leather, paper, pulp, and cosmetics.[79] The aqueous solution of CR exhibits two characteristic peaks at 498 nm ($\pi \rightarrow \pi*$) and 350 nm (n $\rightarrow \pi*$) transitions of the azo group.[80] In the exactly same catalytic reaction steps, 0.3783 g NaBH$_4$ was dissolved in 100 mL double-distilled water in a 250 mL beaker, then 500 μL of CR (1×10^{-2} M) solution was added. Fig. 10b shows the UV/Vis spectrum of CR reduction by NaBH$_4$ in the presence of Cu/0DZnO nanocomposite. After the addition of 0.01 g of the catalyst, the peaks intensities of CR gradually decreased with time, indicating that the catalytic reduction occurred, and the red color completely declined after 3 min. The rate constant was estimated for the slope of the graph that represents the relation between $\ln(A_t/A_0)$ and time (Fig. 10d), and was found to be 1.2 min^{-1}. The Cu/0DZnO nanocomposite acts as an electron delay from BH$_4^-$ (donor) to CR (acceptor) molecules.

3.2.4. Catalytic reduction of acriflavine hydrochloride (ACF). ACF is a fluorescent dye used as a biological stain, topical antiseptic, and in the dual fluorescence analysis of cellular DNA and protein simultaneously. However, inspite of the beneficial uses of this dye, it may be harmful to the eyes or if inhaled. The absorption peak of ACF in aqueous solution is 450 nm. In a typical experiment, 0.3783 g NaBH$_4$ was dissolved in 100 mL double-distilled water in a 250 ml beaker, then 1 mL of ACF (1×10^{-2} M) solution was added. The time-dependent UV/Vis absorption spectra of ACF utilizing NaBH$_4$ in the presence of Cu/0DZnO nanocomposite is displayed in Fig. 10c. After 0.01 g of Cu/0DZnO nanocomposite was added to the reaction mixture, the fluorescent color gradually declined and completely disappeared after 2 min. The calculated rate constant from the slope of the straight line produced from the relationship between $\ln(A_t/A_0)$ and time (Fig. 10d) was found to be 3.81 min^{-1}.

4 Conclusion

Three different ZnO morphologies were successfully synthesized using three different methods (thermal decomposition, microwave-assisted, and precipitation methods). Metallic Cu NPs (5 wt%) were loaded on ZnO nanostructures by a simple reduction method using L-ascorbic acid as a reducing agent. The loading of Cu NPs on ZnO nanostructures leads to a decrease in the optical band gap, slight change in the crystallite sizes, increase in the specific surface area, and increase in the catalytic reduction of 4-NP. The catalytic performance of the nanocomposites takes the following order: Cu/0DZnO > Cu/(1D + 0D) ZnO > Cu/1DZnO. The Cu/0DZnO nanocomposite can reduce 4-NP in a very short time (60 s) with 100% efficiency. The high catalytic performance of this nanocomposite may be attributed to its small particle size, high surface area, and the high distribution of Cu NPs on the surface of ZnO. This composite also showed good catalytic performance in the reduction of organic dyes such as methylene blue, Congo red, and acriflavine hydrochloride. The Cu/0DZnO nanocomposite could be easily recycled with just a minor change in its catalytic activity, indicating its potential for use at a broad scale in chemical process industries.

Data availability

All data generated or analyzed during this study are included in this published article.

Author contributions

Hazim M. Ali: conceptualization, methodology, software, writing – original draft, writing – review & editing. Samia M. Ibrahim: conceptualization, methodology, software, writing – original draft, writing – review & editing. Essam F. Abo Zeid: conceptualization, methodology, writing – review & editing. Ahmed F. Al-Hossainy: conceptualization, methodology, writing – review & editing. Mohamed Abd El-Aal: conceptualization, methodology, writing – original draft, software, validation, writing – review & editing.

Conflicts of interest

The authors declare that they have no known competing financial interests or personal relationships that could have appeared to influence the work reported in this paper.

Acknowledgements

References

1 I. A. Abdelhafeez, S. A. El-Tohamy, M. A. Abd Ul-Malik, S. A. A. Abdel-Raheem and F. M. S. El-Dars, *Curr. Chem. Lett.*, 2022, **11**, 43–62.

2 A. N. Chishti, L. Ni, F. Guo, X. Lin, Y. Liu, H. Wu, M. Chen and G. W. Diao, *J. Environ. Chem. Eng.*, 2021, **9**, 104948.

3 K. Subalakshmi, K. A. Kumar and J. Senthilselvan, *AIP Conf. Proc.*, 2017, **1832**, 110057.

4 A. A. Yahya, K. T. Rashid, M. Y. Ghadhban, N. E. Mousa, H. S. Majdi, I. K. Salih and Q. F. Alsalhy, *Membr*, 2021, 11.

5 A. Nezamzadeh-Ejhieh and S. Khorsandi, *J. Ind. Eng. Chem.*, 2014, **20**, 937–946.

6 M. Trapido and J. Kallas, *Environ. Technol.*, 2000, **21**, 799–808.

7 K. S. Thangamani, N. Muthulakshmi Andal, E. Ranjith Kumar and M. Saravanabhavan, *J. Environ. Chem. Eng.*, 2017, **5**, 2820–2829.

8 M. Kornaros and G. Lyberatos, *J. Hazard. Mater.*, 2006, **136**, 95–102.

9 S. Xie, P. Huang, J. J. Kruzic, X. Zeng and H. Qian, *Sci. Rep.*, 2016, **6**, 21947.

10 A. F. Baye, R. Appiah-Ntiamoah and H. Kim, *Sci. Total Environ.*, 2020, **712**, 135492.

11 M. T. Alula, B. A. Aragaw, S. T. Modukanele and J. Yang, *Inorg. Chem. Commun.*, 2021, **127**, 108504.

12 M. S. Bashir, X. Jiang and X. Z. Kong, *Eur. Polym. J.*, 2020, **129**, 109652.

13 S. Ni, L. Yang, H. Qu, X. Zhu, Z. Xu, M. Yuan, H. Xing, L. Wang, J. Yu and H. Liu, *J. Environ. Chem. Eng.*, 2021, **9**, 105101.

14 B. L. Ryland, S. D. McCann, T. C. Brunold and S. S. Stahl, *J. Am. Chem. Soc.*, 2014, **136**, 12166–12173.

15 B. Eren, C. Heine, H. Bluhm, G. A. Somorjai and M. Salmeron, *J. Am. Chem. Soc.*, 2015, **137**, 11186–11190.

16 M. Donnard and N. Blanchard, *Copper-Mediated Cross-Coupling React.*, 2013, 683–723.

17 G. Sekar, S. Sangeetha, A. Nandy and R. Saha, *Copper Catal. Org. Synth.*, 2020, 395–422.

18 Z. Xie, Y. Cai, H. Hu, C. Lin, J. Jiang, Z. Chen, L. Wang and Y. Pan, *Org. Lett.*, 2013, **15**, 4600–4603.

19 S. Thapa, B. Shrestha, S. K. Gurung and R. Giri, *Org. Biomol. Chem.*, 2015, **13**, 4816–4827.

20 L. Hang, Y. Zhao, H. Zhang, G. Liu, W. Cai, Y. Li and L. Qu, *Acta Mater.*, 2016, **105**, 59–67.

21 H. Sun, A. B. Abdeta, O. A. Zelekew, Y. Guo, J. Zhang, D.-H. Kuo, J. Lin and X. Chen, *J. Mol. Liq.*, 2020, **313**, 113567.

22 T. Kamal, A. M. Asiri and N. Ali, *Spectrochim. Acta, Part A*, 2021, **261**, 120019.

23 R. Xu, H. Bi, G. He, J. Zhu and H. Chen, *Mater. Res. Bull.*, 2014, **57**, 190–196.

24 A. A. Kassem, H. N. Abdelhamid, D. M. Fouad and S. A. Ibrahim, *J. Environ. Chem. Eng.*, 2021, **9**, 104401.

25 M. T. Islam, N. Dominguez, M. A. Ahsan, H. Dominguez-Cisneros, P. Zuniga, P. J. J. Alvarez and J. C. Noveron, *J. Environ. Chem. Eng.*, 2017, **5**, 4185–4193.

26 S. A. Rasaki, C. Zhao, R. Wang, J. Wang, H. Jiang and M. Yang, *Mater. Res. Bull.*, 2019, **119**, 110536.

27 H. A. Oualid, O. Amadine, Y. Essamlali, I. M. Kadmiri, H. El Arroussi and M. Zahouily, *Nanoscale Adv.*, 2019, **1**, 3151–3163.

28 G. García-Valdivieso, E. Arenas-Sánchez, P. Horta-Fraijo, A. Simakov, H. R. Navarro-Contreras and B. Acosta, *Nanotechnology*, 2021, **32**, 315713.

29 M. Behera, N. Tiwari, A. Basu, S. Rekha Mishra, S. Banerjee, S. Chakrabortty and S. K. Tripathy, *Adv. Powder Technol.*, 2021, **32**, 2905–2915.

30 M. Bordbar, N. Negahdar and M. Nasrollahzadeh, *Sep. Purif. Technol.*, 2018, **191**, 295–300.

31 F. S. Alamro, A. M. Mostafa, H. A. Ahmed and A. Toghan, *Surf. Interfaces*, 2021, **26**, 101406.

32 A. M. Mostafa and E. A. Mwafy, *J. Mol. Struct.*, 2020, **1221**, 128872.

33 M. T. Alula, P. Lemmens and M. L. Madingwane, *Microchem. J.*, 2020, **156**, 104976.

34 Y. Sun, L. Chen, Y. Bao, Y. Zhang, J. Wang, M. Fu, J. Wu and D. Ye, *Catalysis*, 2016, **6**, 188.

35 K. H. Ernst, A. Ludviksson, R. Zhang, J. Yoshihara and C. T. Campbell, *Phys. Rev. B*, 1993, **47**, 13782–13796.

36 G. P. Singh and M. K. Roy, *Mater. Today: Proc.*, 2021, **46**, 5878–5880.

37 S. K. Nikhil, A. Das, P. M. Kumar, M. Bhagavathiachari and R. G. Nair, *Opt. Mater.*, 2021, **121**, 111551.

38 D. Cao, S. Gong, X. Shu, D. Zhu and S. Liang, *Nanoscale Res. Lett.*, 2019, **14**, 210.

39 Q. Liu, T. Yasunami, K. Kuruda and M. Okido, *Trans. Nonferrous Met. Soc. China*, 2012, **22**, 2198–2203.

40 M. Abd El-Aal and T. Seto, *Res. Chem. Intermed.*, 2020, **46**, 3741–3756.

41 P. Fageria, S. Gangopadhyay and S. Pande, *RSC Adv.*, 2014, **4**, 24962–24972.

42 M. A. El-Aal, T. Seto and A. Matsuki, *Appl. Phys. A*, 2020, **126**, 572.

43 W. Z. Tawfik, Z. S. Khalifa, M. S. Abdel-wahab and A. H. Hammad, *J. Mater. Sci.: Mater. Electron.*, 2019, **30**, 1275–1281.

44 E. F. A. Zeid, I. A. Ibrahem, W. A. A. Mohamed and A. M. Ali, *Mater. Res. Express*, 2020, **7**, 26201.

45 E. Gurgur, S. S. Oluyamo, A. O. Adetuyi, O. I. Omotunde and A. E. Okoronkwo, *SN Appl. Sci.*, 2020, **2**, 911.

46 M. Chakraborty, A. Ghosh and R. Thangavel, *J. Sol-Gel Sci. Technol.*, 2015, **74**, 756–764.

47 O. I. Omotunde, A. E. Okoronkwo, A. F. Aiyesanmi and E. Gurgur, *J. Photochem. Photobiol., A*, 2018, **365**, 145–150.

48 A. Ghosh, N. Kumari and A. Bhattacharjee, *Pramana*, 2015, **84**, 621–635.

49 M. Sathya and K. Pushpanathan, *Appl. Surf. Sci.*, 2018, **449**, 346–357.

50 A. Modwi, K. K. Taha, L. Khezami, A. S. Al-Ayed, O. K. Al-Duaij, M. Khairy and M. Bououdina, *J. Inorg. Organomet. Polym. Mater.*, 2020, **30**, 2633–2644.

51 T. Chitradevi, A. Jestin Lenus and N. Victor Jaya, *Mater. Res. Express*, 2019, **7**, 15011.

52 A. A. Othman, M. A. Osman, E. M. M. Ibrahim, M. A. Ali and A. G. Abd-Elrahim, *Mater. Sci. Eng., B*, 2017, **219**, 1–9.

53 S. Ebrahimiasl, A. Zakaria, A. Kassim and S. N. Basri, *Int. J. Nanomed.*, 2015, **10**, 217–227.

54 J. Liu, Y. Chen and H. Zhang, *Sensors*, 2021, 21.

55 V. Sreeja, K. N. Jayaprabha and P. A. Joy, *Appl. Nanosci.*, 2015, **5**, 435–441.

56 V. U. Siddiqui, A. Ansari, M. T. Ansari, M. K. Akram, W. A. Siddiqi, A. M. Alosaimi, M. A. Hussein and M. Rafatullah, *Catalysis*, 2021, 11.

57 T. R. Chetia, M. S. Ansari and M. Qureshi, *ACS Appl. Mater. Interfaces*, 2015, **7**, 13266–13279.

58 E. C. Arvaniti, M. C. G. Juenger, S. A. Bernal, J. Duchesne, L. Courard, S. Leroy, J. L. Provis, A. Klemm and N. De Belie, *Mater. Struct.*, 2015, **48**, 3687–3701.

59 A. E.-A. A. Said, M. M. M. Abd El-Wahab and M. Abd El-Aal, *Monatsh. Chem.*, 2016, **147**, 1507–1516.

60 S. S. Patil, M. G. Mali, M. S. Tamboli, D. R. Patil, M. V Kulkarni, H. Yoon, H. Kim, S. S. Al-Deyab, S. S. Yoon, S. S. Kolekar and B. B. Kale, *Catal. Today*, 2016, **260**, 126–134.

61 H. Nie, L. Fu, J. Zhu, W. Yang, D. Li and L. Zhou, *Mater*, 2018, 11.

62 G. Qu, G. Fan, M. Zhou, X. Rong, T. Li, R. Zhang, J. Sun and D. Chen, *ACS Omega*, 2019, **4**, 4221–4232.

63 X. Kang, D. Teng, S. Wu, Z. Tian, J. Liu, P. Li, Y. Ma and C. Liang, *J. Colloid Interface Sci.*, 2020, **566**, 265–270.

64 P. Deka, R. C. Deka and P. Bharali, *New J. Chem.*, 2014, **38**, 1789–1793.

65 S. Haider, T. Kamal, S. B. Khan, M. Omer, A. Haider, F. U. Khan and A. M. Asiri, *Appl. Surf. Sci.*, 2016, **387**, 1154–1161.

66 S. Ghosh, R. Das, I. H. Chowdhury, P. Bhanja and M. K. Naskar, *RSC Adv.*, 2015, **5**, 101519–101524.

67 S. Gao, X. Jia, J. Yang and X. Wei, *J. Mater. Chem.*, 2012, **22**, 21733–21739.

68 P. Zhang, Y. Sui, G. Xiao, Y. Wang, C. Wang, B. Liu, G. Zou and B. Zou, *J. Mater. Chem. A*, 2013, **1**, 1632–1638.

69 J. Jiang, Y. Soo Lim, S. Park, S.-H. Kim, S. Yoon and L. Piao, *Nanoscale*, 2017, **9**, 3873–3880.

70 Y. Sun, L. Xu, Z. Yin and X. Song, *J. Mater. Chem. A*, 2013, **1**, 12361–12370.

71 J. Jiang, G. H. Gunasekar, S. Park, S.-H. Kim, S. Yoon and L. Piao, *Mater. Res. Bull.*, 2018, **100**, 184–190.

72 S. Wang, S. Gao, Y. Tang, L. Wang, D. Jia and L. Liu, *J. Solid State Chem.*, 2018, **260**, 117–123.

73 C.-C. Yeh, P.-R. Wu and D.-H. Chen, *Mater. Lett.*, 2014, **136**, 274–277.

74 Z.-Y. Xiao, S.-R. Zhai, X.-P. Ma, Z.-Y. Zhao, X. Wang, H. Bai and Q.-D. An, *New J. Chem.*, 2017, **41**, 13230–13234.

75 M. Nasrollahzadeh, Z. Issaabadi and S. M. Sajadi, *RSC Adv.*, 2018, **8**, 3723–3735.

76 W. Liu, K. Tian, H. Jiang and H. Yu, *Green Chem.*, 2014, 4198–4205.

77 S. A. Hira, H. S. Hui, M. Yusuf and K. H. Park, *Catal. Commun.*, 2020, **141**, 106011.

78 B. R. Ganapuram, M. Alle, R. Dadigala, A. Dasari, V. Maragoni and V. Guttena, *Int. Nano Lett.*, 2015, **5**, 215–222.

79 K. Naseem, Z. H. Farooqi, R. Begum and A. Irfan, *J. Cleaner Prod.*, 2018, **187**, 296–307.

80 F. Farzaneh and S. Haghshenas, *Mater. Sci. Appl.*, 2012, **03**, 697–703.